Multiple shells around G79.29+0.46 revealed from near-IR to millimeter data

F. M. Jiménez-Esteban[1,2,3], J. R. Rizzo[4,5] and Aina Palau[6]

fran.jimenez-esteban@cab.inta-csic.es

ABSTRACT

Aiming to perform a study of the warm dust and gas in the luminous blue variable star G79.29+0.46 and its associated nebula, we present infrared Spitzer imaging and spectroscopy, and new CO $J = 2 \to 1$ and $4 \to 3$ maps obtained with the IRAM 30m radio telescope and with the Submillimeter Telescope, respectively. We have analyzed the nebula detecting multiple shells of dust and gas connected to the star. Using Infrared Spectrograph–Spitzer spectra, we have compared the properties of the central object, the nebula, and their surroundings. These spectra show a rich variety of solid-state features (amorphous silicates, polycyclic aromatic hydrocarbons, and CO_2 ices) and narrow emission lines, superimposed on a thermal continuum. We have also analyzed the physical conditions of the nebula, which point to the existence of a photo-dissociation region.

Subject headings: circumstellar matter – dust, extinction – ISM: individual objects (G79.29+0.46) – ISM: lines and bands – stars: evolution – stars: mass-loss

1. Introduction

Luminous blue variable (LBV) stars are massive objects which, as they evolve from the main sequence, undergo a short period of extremely high mass loss (up to $10^{-3} M_\odot \, \mathrm{yr}^{-1}$), sometimes accompanied by so-called giant eruptions, such as the well-known nineteenth-century outburst of η Car (Smith & Owocki 2006). This mass-loss strongly influences the further stellar evolution and leads to the formation of extended circumstel-

lar nebula (see Humphreys & Davidson 1994, for a review). Clark et al. (2005) reported a total of 12 galactic LBV stars and 23 LBV candidates. From the whole sample, however, only 20 have nebular circumstellar emission. Such nebulae have both gaseous and dusty components, and two kinds of geometry, spherical and bipolar, have been recognized.

Since LBV nebulae are strong emitters in the mid- and far-infrared, the physical and chemical conditions of the material surrounding LBV stars can be traced studying their spectral characteristics in this wavelength range. Thus, a few of these nebulae were spectroscopically studied with the Infrared Space Observatory (*ISO*) satellite, revealing the presence of solid-state features characteristic of polycyclic aromatic hydrocarbons (PAHs) and silicate dust in both forms, amorphous and crystalline (e.g. Lamers et al. 1996a; Voors et al. 1999, 2000b). Together with these, numerous forbidden lines on top of a smooth continuum were detected (e.g. Lamers et al. 1996b).

With the advent of *Spitzer Space Telescope* (Werner et al. 2004), unprecedented high sensitiv-

[1]Centro de Astrobiología (CSIC-INTA), P.O. Box 78, E-28691, Villanueva de la Cañada, Madrid, Spain

[2]Spanish Virtual Observatory

[3]Saint Louis University, Madrid Campus, Division of Science and Engineering, Avda. del Valle 34, E-28003 Madrid, Spain

[4]Centro de Astrobiología (CSIC-INTA), Laboratorio de Astrofísica Molecular, Ctra. de Ajalvir km. 4, E-28850 Torrejón de Ardoz, Spain

[5]Escuela Superior Politécnica, Universidad Europea de Madrid, Urb. El Bosque, E-28670 Villaviciosa de Odón, Spain

[6]Institut de Ciències de l'Espai (CSIC-IEEC), Campus UAB, Facultat de Ciències, Torre C-5 parell, E-08193 Bellaterra, Barcelona, Spain

arXiv:1003.4455v2 [astro-ph.SR] 24 Mar 2010

ity and resolution imaging and spectroscopy have been possible in the infrared, making feasible the study of LBV nebulae with much great detail. Thus, recently new works have been published (Morris, P., et al. 2008; Smith 2007; Umana et al. 2009; Gvaramadze et al. 2009) based on these new data, which have represented an important step forward in the knowledge of this brief evolutionary phase of high-mass stars.

The molecular gas in LBV nebulae is also a subject of interest. It may trace radiatively affected and/or shocked regions, which may tell us about the evolution of the progenitor star. In addition, the chemical evolution and the formation of circumstellar molecular gas may also be determined by molecular studies. Gaseous CO was firstly detected around the AG Car nebula (Nota et al. 2002), and after then in some other objects (Rizzo et al. 2008a). Highly excited ammonia was also detected in the Homunculus Nebula (Smith et al. 2006).

Concerning the molecular counterpart, the most studied source is G79.29+0.46 (Rizzo et al. 2008b, hereafter Paper I). In this object, the detection of the CO $J = 3 \rightarrow 2$ line surrounding the nebula unveiled the presence of moderately dense ($10^4 - 10^5 \, \text{cm}^{-3}$) CO gas, probably affected by a C-shock at a velocity of $\sim 15 \, \text{km s}^{-1}$. This CO-ring-like structure has a diameter of $\sim 3'.2$, and it is strikingly homogeneous in shape.

The origin of the nebula of G79.29+0.46 is not clear. From Very Large Array (*VLA*) observations of radio continuum and H I, Higgs et al. (1994) showed the thermal nature of the continuum emission and suggested that the nebula is an ionized shell of $\sim 15 \, M_{\odot}$ of swept-up interstellar material. However, after examining the *IRAS* high-resolution images of G79.29+0.46, Waters et al. (1996) concluded that it is a detached shell due to an epoch of high mass loss ($\sim 5 \times 10^{-4} \, M_{\odot} \, \text{yr}^{-1}$) during the red supergiant or LBV phase, followed by a less intense mass-loss period.

Concerning the central object, it has been spectroscopically studied in the optical and in the near-infrared wavelength range (Waters et al. 1996; Voors et al. 2000b). Its LBV classification is supported by the high luminosity ($> 10^5 \, L_{\odot}$), the moderate stellar wind ($94 - 110 \, \text{km s}^{-1}$), and the current high mass-loss rate ($10^{-6} \, M_{\odot} \, \text{yr}^{-1}$) (Waters et al. 1996). Unfortunately, its effective

temperature (T_{eff}) is not well-known because it is highly model dependent. The detection of a He I emission line near Brα (Waters et al. 1996) suggests a T_{eff} well above 10,000 K. On the other hand, the LBV nature of the central star may limit the T_{eff} to a maximum of 30,000 K.

In Paper I, a careful discussion about the distance to G79.29+0.46 was done. We will assume a distance of 1.7 kpc throughout all the paper.

The fingerprint of stellar evolution onto the circumstellar/interstellar medium (ISM) can provide a valuable input to learn about the processes, which govern the star itself and also affect the evolution of the surrounding gas and dust. The aim of this paper is to trace the distribution of warm dust, PAHs, and gaseous CO in relation with G79.29+0.46 and its associated nebula. To do this, we present infrared Spitzer imaging and spectroscopy, and new submillimeter CO $J = 2 \rightarrow 1$ and $4 \rightarrow 3$ maps obtained with the IRAM 30m radio telescope and the Submillimeter Telescope (*SMT*), respectively. In comparison to Paper I, this new data set improves the angular resolution and the analysis of the physical conditions.

2. Spitzer data

The Spitzer data used in this paper have been obtained from the public Spitzer archive[1].

2.1. Imaging

Two cameras are on board of Spitzer: the InfraRed Array Camera (IRAC; Fazio et al. 2004) and the Multiband Imaging Photometer (MIPS; Rieke et al. 2004), which provide imaging capability from 3 to 200 μm.

Near-infrared images were obtained on 2007 July 05 using the four IRAC bands at 3.6, 4.5, 5.8, and 8.0 μm, as part of the program 30188 (AOR 17330688). Mid-infrared images at 24 and 70 μm were also obtained using MIPS as part of the program 40184 (AOR 22510592) on 2007 December 02. We have worked with the standard post-BCD data sets, for both IRAC and MIPS images, as retrieved with Leopard from the Spitzer archive. They were processed with the version S16.1.0 and S16.1.1, respectively. Aladin[2] was

---

[1] http://archive.spitzer.caltech.edu
[2] http://aladin.u-strasbg.fr

used to cut the images to show a field of view of $9' \times 9'$ centered on the LBV star. These images are shown in Figure 1. The brightness scale of every filter has been individually selected to better investigate the nebular emission of G79.29+0.46.

2.2. IRS Spectra

The *Spitzer* satellite has a third instrument on board, the Infrared Spectrograph (IRS; Houck et al. 2004). It provides crucial spectroscopic information in the wavelength range from 5 to $40\,\mu$m.

Three targets in the field of G79.29+0.46 have been spectroscopically observed in four observational programs: a target including the exciting star and its surroundings (hereafter called 'the central object'), a target centered at a position where the ring nebula is most prominent (hereafter called 'the shell'), and a nearby infrared dark cloud (hereafter called 'the IRDC'). These observations are tabulated in Table 1, and the positions of the IRS slits are shown in Figure 2. It should be noted that all three, the central object, the shell, and the IRDC, include emission from nearby regions than the targets themselves.

The spectra were obtained by using all possible modules: short–low (SL), short–high (SH), long–low (LL), and long–high (LH). There are low-resolution spectra (SL and LL) for the three studied targets, which cover the spectral range from 5.2 to $38.0\,\mu$m. However, high-resolution spectra (SH and LH), covering the spectral range from 9.2 to $37.2\,\mu$m, are only available for the central object. We have worked with the standard post-BCD data sets. We have cleaned the resulting one-dimensional spectra for residual bad pixels flagged by the pipeline and visually inspected to identify spurious jumps and glitches. No spurious jumps were detected and the glitches found were interpolated. Finally, we have merged the different orders of each module into one final spectrum per module using an IDL code developed to this end. We have not corrected for basic aperture and slit loss. Spectra are shown in Figures 3 – 5.

In the case of the central object, the target has been observed on three different occasions (see Table 1). The first time (AOR 7557888), the IRS slits were not correctly positioned over the central object. The second time (AOR 9761024), there should have been a flux calibration prob-

lem, since the two orders do not match. The third time (AOR 17333248), the data do not show any problem. Thus, we have used these last spectra for the analysis, corresponding with the modules SL, SH, and LH. However, on this last occasion LL spectrum was not taken, so we have used for the analysis the LL spectrum corresponding to the AOR 9761024. The SL spectrum of the AOR 9761024 and those of the AOR 7557888 have been used to confirm the detection of the solid spectral features and the emission lines (see Section 4.3).

3. CO observations

3.1. CO $J = 2 \rightarrow 1$ Line Emission

We used the IRAM 30m radio telescope at Pico Veleta (Spain) in 2008 February, to map the CO $J = 2 \rightarrow 1$ line emission in a region of $\sim 7' \times 7'$ around G79.29+0.46. The front end was the nine-beam HERA receiver (Schuster et al. 2004). In order to optimize both observing time and sampling, we used the *on-the-fly* mode. A total of four individual maps, in orthogonal sampling directions, were obtained and later combined in a single data cube using the GILDAS package. The VESPA autocorrelator was used as back end, in frequency switching mode. The final bandwidth was $44\,$MHz (equivalent to $\sim 57\,$km s^{-1} at the rest frequency), and the spectral resolution was $80\,$kHz ($\sim 0.1\,$km s^{-1}). Due to the frequency switching, mesospheric CO emission had to be removed from all the spectra. After folding, low-order polynomials were fitted to remove baselines using CLASS software package (also included in GILDAS). Typical rms was $0.2\,$K, in T_A^* scale.

Calibration was performed during the observations using two absorbers at different temperatures and later checked up on standard sources (Mauersberger et al. 1989). The uncertainty in calibration is below 15%. The angular resolution of the radio telescope at $230\,$GHz half-power beam width (HPBW) is $11''$. However, we have further degraded the final map down to $18''$, in order to reduce the map noise and to get the same HPBW corresponding to the CO $J = 4 \rightarrow 3$ map.

Some other emission lines were observed during the same observing session. The results from these lines will be released in a future paper (J. R. Rizzo et al. 2010, in preparation), together with a more
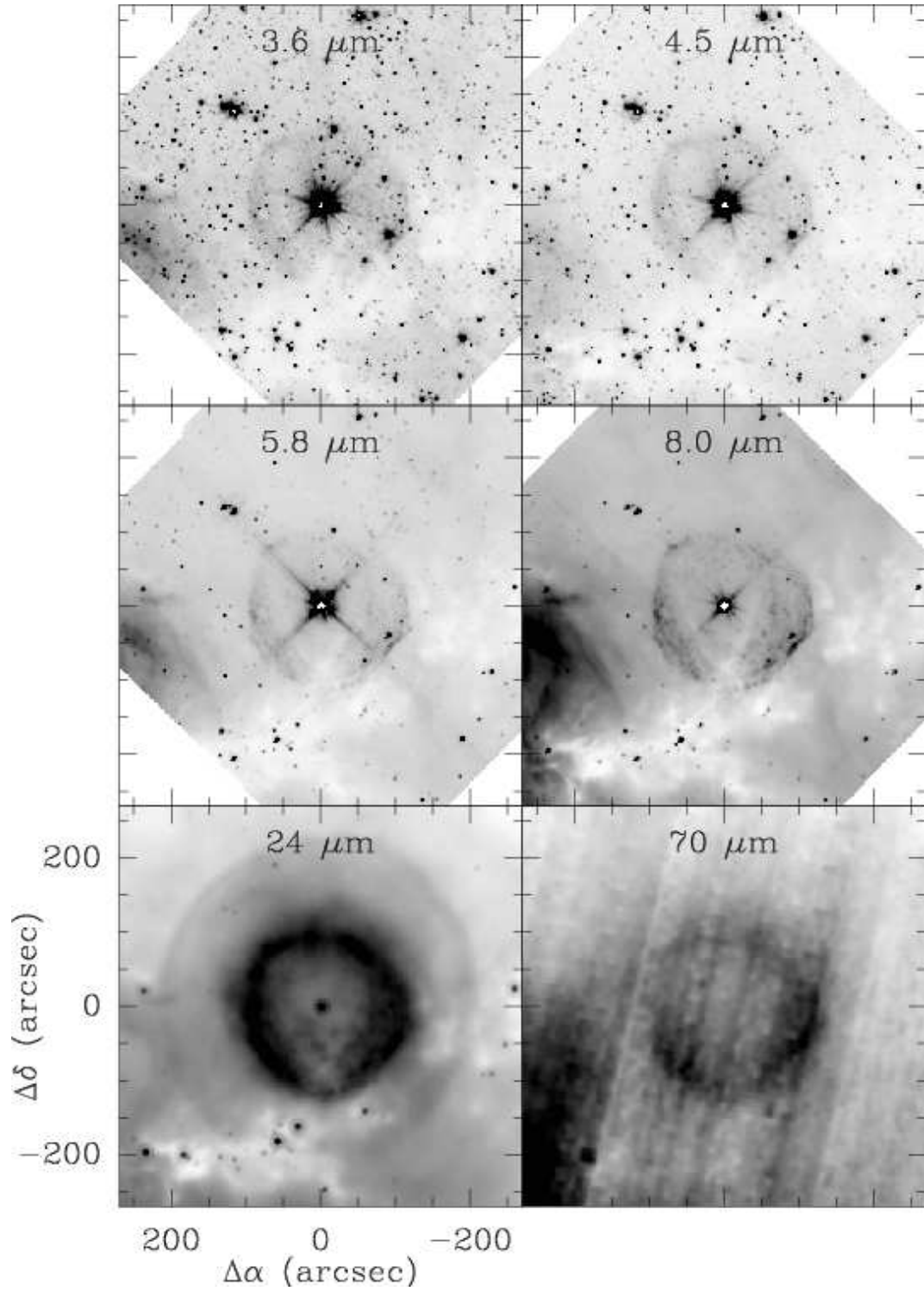
Fig. 1.— Spitzer images of G79.29+0.46. Wavelengths are indicated at the upper part of each image, and angular offsets are referred to the central star, at (R.A., decl.)$_{J2000}$ = ($20^h31^m42\overset{s}{.}3, +40°21'58''$). A linear brightness scale has been artificially selected for each individual image to better show weak and diffuse features, instead of point-like objects. Note an outer thin second shell clearly visible only at $24\,\mu m$.
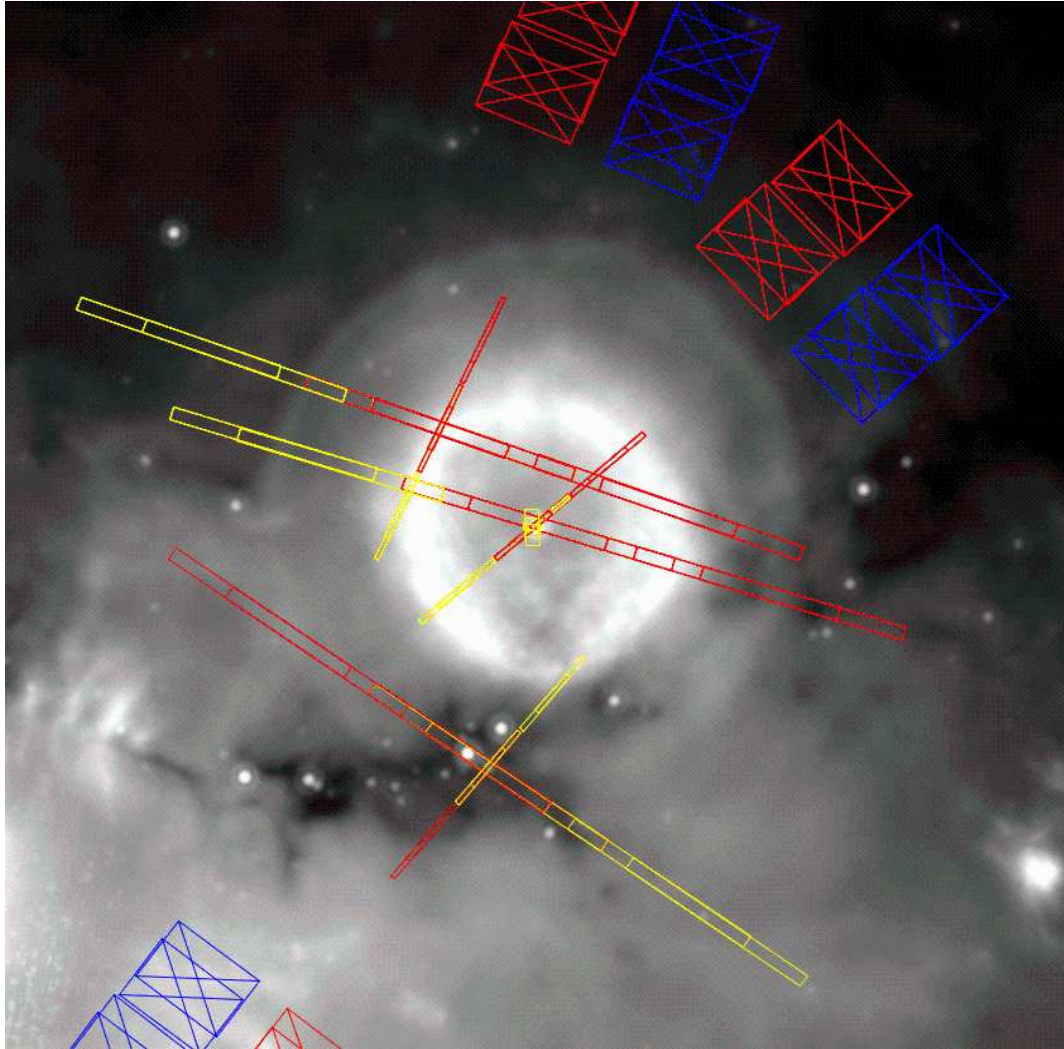
Fig. 2.— Overplot on the MIPS $24\,\mu$m image of the IRS spectral slits for all modules, as shown by Leopard software. The field of view is $14'\times14'$ centered on the LBV star. Only the observations used in the analysis are shown. The three different positions correspond with the central object, the shell, and the IRDC.

TABLE 1

IRS OBSERVATIONS IN THE FIELD OF G79.29+0.46

ID program	AOR	Date	R.A. J(2000)	Decl. J(2000)	Target	Module	λ Range (μm)	Slit Size (arcsec)	Pipeline
666	7557888	2003 Nov 14	$20^h\ 31^m\ 42^s.0$	$+40°\ 21'\ 42''.0$	The central object	SL	$5.2-14.5$	3.6×57	s15.3.0
						SH	$9.9-19.6$	4.7×11.3	s15.3.0
						LL	$14.0-38.0$	10.5×168	s17.2.0
1407	9761024	2004 May 11	$20^h\ 31^m\ 42^s.1$	$+40°\ 21'\ 58''.8$	The central object	SL	$5.2-14.5$	3.6×57	s15.3.0
						LL	$14.0-38.0$	10.5×168	s17.2.0
	9761280	2004 May 14	$20^h\ 31^m\ 48^s.9$	$+40°\ 23'\ 15''.4$	The shell	SL	$5.2-14.5$	3.6×57	s15.3.0
						LL	$14.0-38.0$	10.5×168	s17.2.0
3121	12096768	2004 Dec 07	$20^h\ 31^m\ 45^s.6$	$+40°\ 18'\ 43''.6$	The IRDC	SL	$5.2-14.5$	3.6×57	s15.3.0
						LL	$14.0-38.0$	10.5×168	s17.2.0
30188	17333248	2006 Jun 28	$20^h\ 31^m\ 42^s.5$	$+40°\ 21'\ 56''.0$	The central object	SL	$5.2-14.5$	3.6×57	s15.3.0
						SH	$9.9-19.6$	4.7×11.3	s15.3.0
						LH	$18.7-37.2$	11.1×22.3	s17.2.0

complete analysis of the CO $J=2\rightarrow1$ results.

3.2. CO $J=4\rightarrow3$ Line Emission

The observations of the CO $J=4\rightarrow3$ line were made in 2006 June with the SMT, located on Mount Graham, Arizona. The telescope is a 10.4 m diameter primary with a nutating secondary. Design, optics, and structural aspects of the telescope were extensively described by Baars et al. (1999). The single-channel receiver SORAL-490 was used under excellent weather conditions ($\tau_{461\,GHz} \sim 0.4-0.5$). As the back end, we used one of the acousto-optical spectrometers (AOSCs), which provides an usable bandwidth of about 250 MHz (corresponding to 162 km s^{-1} of coverage), and a spectral resolution of 367 kHz (0.24 km s^{-1}).

The receiver was calibrated with ambient temperature and a liquid nitrogen-cooled absorbing load. Calibration of the final data has uncertainties below 20 %. System temperature was measured with the standard sky/ambient temperature load method (Kutner & Ulich 1981). Calibrations were performed every 15 – 20 minutes to track variations in atmospheric opacity. Typical system temperature during the observations was in the range of 1000 – 1200 K, depending on the elevation and the atmospheric opacity.

The pointing was checked within 2 hr on a planet or other bright continuum source. Corrections to the pointing model were not more than 4$''$ in either azimuth or elevation. Planet observations were also used to compute the main-beam efficiency at the observed frequency.

Only a small area toward the southwest of G79.29+0.46 was observed, where the most interesting CO features appear (Paper I). Position switching was employed, using the same reference position for all observed points. Due to time restriction, the CO $J=4\rightarrow3$ map was sampled only by one beam (18$''$) in both equatorial coordinates, and hence it is not fully sampled. The reduction processes were similar to those of IRAM's data, already described in Section 3.1.

4. Results

4.1. Infrared images

The distance assumed for G79.29+0.46 is consistent with its probable identification as a member of Cyg OB2. Located at the southern part and close to the border of Cyg OB2, G79.29+0.46 is behind the Great Cygnus Rift, just to the northwest of the intense radio source DR 15, which causes high visual extinction from 4 to at least 10 mag. Thus, the infrared emission of G79.29+0.46 is expected to be heavily contaminated by foreground/background emission, as it is clearly noticeable in all Spitzer images. In addition, a large-scale infrared emission is also present toward the east of the images. This large-scale emission increases its relative intensity with respect to the background with the wavelength, and is similar to the large-scale CO gas emission noted in Paper I at millimeter and submillimeter wavelengths. It was related to the cloud around DR 15 (Oka et al. 2001). Due to this strong contamina-
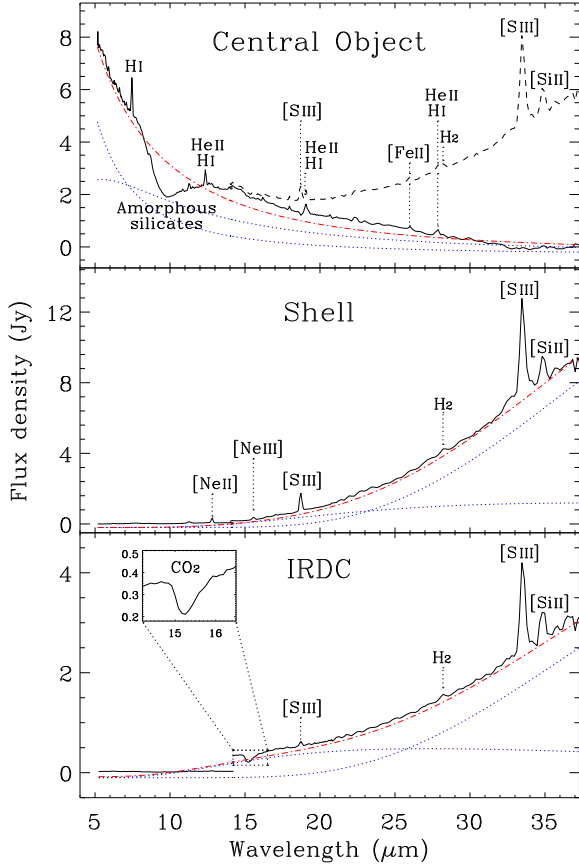
Fig. 3.— IRS low-resolution spectra (modules SL and LL) of the three studied targets. The most prominent spectral lines and solid features are labeled in the figure. *Upper panel*: the spectra of the central object after subtracting the LL spectrum of the shell (see the text). The dashed line corresponds to the original LL spectrum. The dotted (blue) lines correspond to the emission of two blackbodies, one at $20,000\,K$ and the other at $925\,K$. The dash-dotted (red) line is the combination of these two blackbodies. *Middle panel*: the spectra of the shell. The dotted (blue) lines correspond to the emission of two blackbodies, one at $65\,K$ and the other at $132\,K$. The dash-dotted (red) line is the combination of these two blackbodies. *Lower panel*: the spectra of the IRDC. The dotted (blue) lines correspond to the emission of two blackbodies, one at $66\,K$ and the other at $187\,K$. The dash-dotted (red) line is the combination of these two blackbodies.
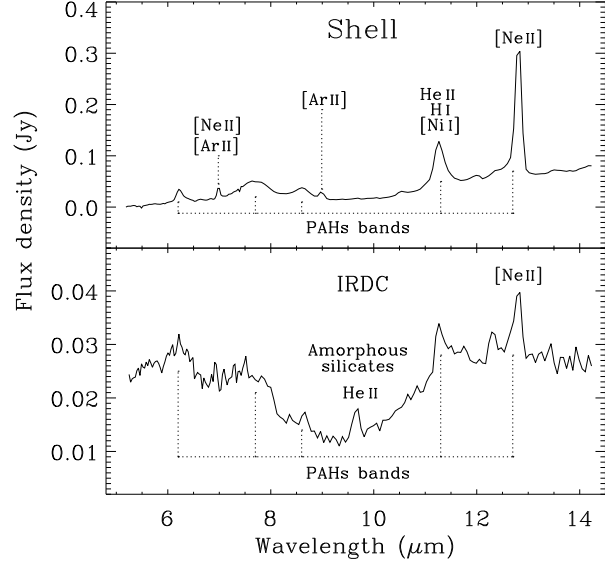

Fig. 4.— IRS SL module spectra of the shell and the IRDC. The most prominent spectral lines and solid bands are labeled in the figure.
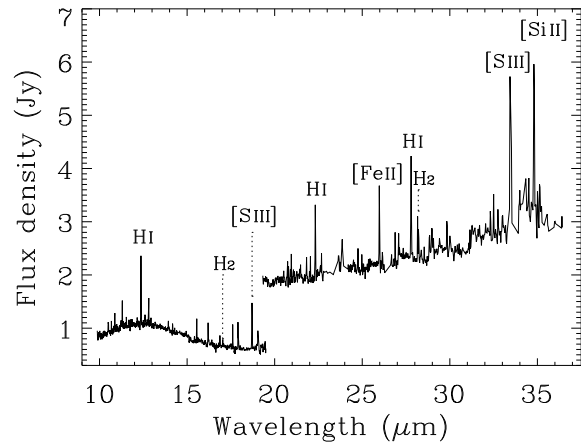

Fig. 5.— IRS high-resolution spectra (modules SH and LH) of the central object. The most prominent spectral lines are labeled in the figure.

7

tion, we refrain from computing the dust mass, as it is a hard task and the results might not be reliable enough.

The central object is detected in all Spitzer bands but MIPS $70\,\mu$m. We used MOPEX supported software to perform point-spread function (PSF) photometry in the MIPS $24\,\mu$m image, obtaining a flux density of $0.89\,$Jy for the central object. Due to saturation problems, it was not possible to obtain the fluxes of the central object at shorter wavelengths.

The ring nebula previously detected by the *IRAS* and Midcourse Space Experiment (*MSX*) satellites (Waters et al. 1996; Egan et al. 2002) is discernible from 3.6 to $70\,\mu$m. The nebular emission dominates the image at $24\,\mu$m, being just above the background level at shorter and longer wavelengths. The nebula presents a pretty spherical shape with a diameter of $\sim 3\rlap.'7$ ($\sim 1.8\,$pc). The shell looks like incomplete to the south, probably due to a foreground IRDC, which is known to possess a very large visual extinction (Redman et al. 2003). However, it is not clear whether this IRDC is part of the large complex including DR 15 or it is an unrelated foreground cloud (Egan et al. 1998).

Thanks to the high angular resolution and sensitivity of these Spitzer images, we have discovered an outstanding new, outer shell with almost spherical shape as well. This outer shell is only visible in the $24\,\mu$m image (Figure 1) and has a diameter of $\sim 6\rlap.'8$, ($\sim 3.4\,$pc). During the process of writing this paper, Gvaramadze et al. (2009) reported a diffuse halo associated with G79.29+0.46, which corresponds to the inside of this newly discovered shell.

4.2.   CO maps

As we show below, the CO data shown here improve the results gathered in Paper I, due to a higher angular resolution and lower rms noise compared to those in Paper I, providing a higher signal-to-noise ratio (S/N). In addition, mapping the CO $J = 4 \rightarrow 3$ line emission allows us to test a wider range of excitation conditions, due to the higher energy levels involved and the critical density needed to excite this line. According to the aim of this work, here we provide the most relevant morphological features, postponing a more detailed dynamical study to a future paper

(J. R. Rizzo et al. 2010, in preparation).

The whole velocity range of emission in the $J = 2 \rightarrow 1$ line goes from -25 to $15\,$km s^{-1}. The most intense emission corresponds to the Local Arm, where the confusion effects are presumably the highest. The most outstanding features in relation to G79.29+0.46 appear in velocity ranges similar to those shown in Paper I (see Figure 4 of that paper). Figures 6 and 7 show the CO $J = 2 \rightarrow 1$ and $4 \rightarrow 3$ distributions in the velocity ranges from -3.2 to -2.6 and from $+3.4$ to $+4.0\,$km s^{-1}, respectively. The CO $J = 2 \rightarrow 1$ line contours are superposed to an image at $24\,\mu$m in gray scale.

For the $J = 2 \rightarrow 1$ data, a Gaussian convolution has been applied, down to a resolution of $18''$. This convolution reduces the noise map and equals the angular resolution of the $J = 4 \rightarrow 3$ line. In both figures, the inset in the $J = 2 \rightarrow 1$ maps corresponds exactly to the mapped area in the $J = 4 \rightarrow 3$ line, shown on the right.

In Figure 6, an arc-like feature dominates the map, in good coincidence with the $24\,\mu$m inner shell, especially in the western half. The $J = 4 \rightarrow 3$ line emission depicts part of a remarkable thin shell, unresolved even at $18''$ of resolution.

The shocked clump, unresolved in Paper I, is clearly seen in Figure 7. In this velocity range, all the emission is outside the $24\,\mu$m inner shell. The southwestern feature, also observed in the $J = 4 \rightarrow 3$ line emission, looks like part of a second CO shell. Note that this feature is located outside the shell shown in Figure 6.

The emission at velocities intermediate to those of Figures 6 and 7 does not show any shell-like pattern, and consequently we think that the two shells are different features, and not the consequence of a mere velocity gradient. Summarizing, at the southwestern part of the field, we see two CO concentric slabs, which fill the space between the two shells detected at $24\,\mu$m.

4.3.   Infrared spectra

The infrared spectral data show a rich variety of solid-state features and narrow emission lines, superimposed on a thermal continuum.

Using the low-resolution IRS spectra, it is possible to study the spectral energy distribution (SED) of the three observed targets (Figure 3).
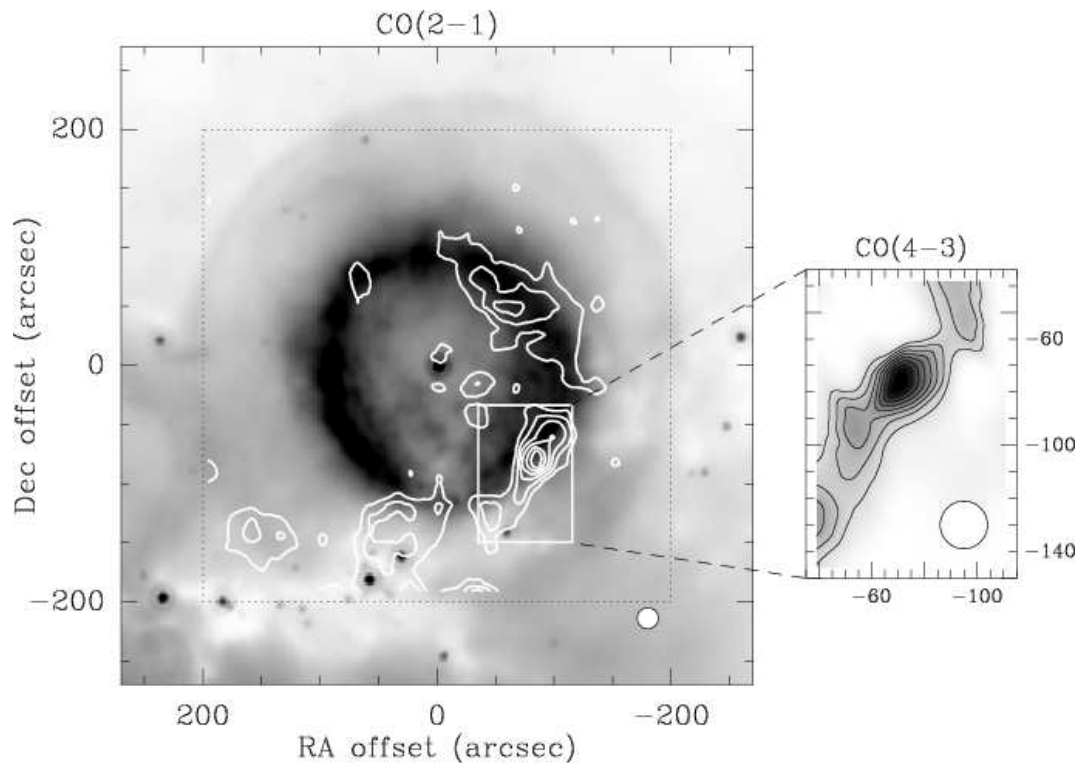
Fig. 6.— *Left:* CO $J=2\rightarrow1$ map in the surroundings of G79.29+0.46, as obtained with the IRAM 30m radio telescope. The map is centered on the LBV star, and the velocity range of integration is from –3.2 to –2.6 km s^{-1}. The pointed square indicates the observed field, and gray scale corresponds to the 24 μm emission. Contours are 40 % – 90 % of the peak value (11.8 K in T_A^* scale), in steps of 10 %. *Right:* CO $J=4\rightarrow3$ map in the same velocity range, corresponding exactly to the inset in the left panel, as obtained with the SMT 10 m radio telescope. The inset has a size of 80″×116″. Contours are 25 % – 95 % of the peak value (1.8 K in T_A^* scale), in steps of 10 %. In both maps, the angular resolutions are shown as white circles in the lower right. It is striking the high correlation of the CO emission in this velocity range with the infrared inner shell. The CO shell is especially thin in the $J=4\rightarrow3$ map, unresolved by the beam.
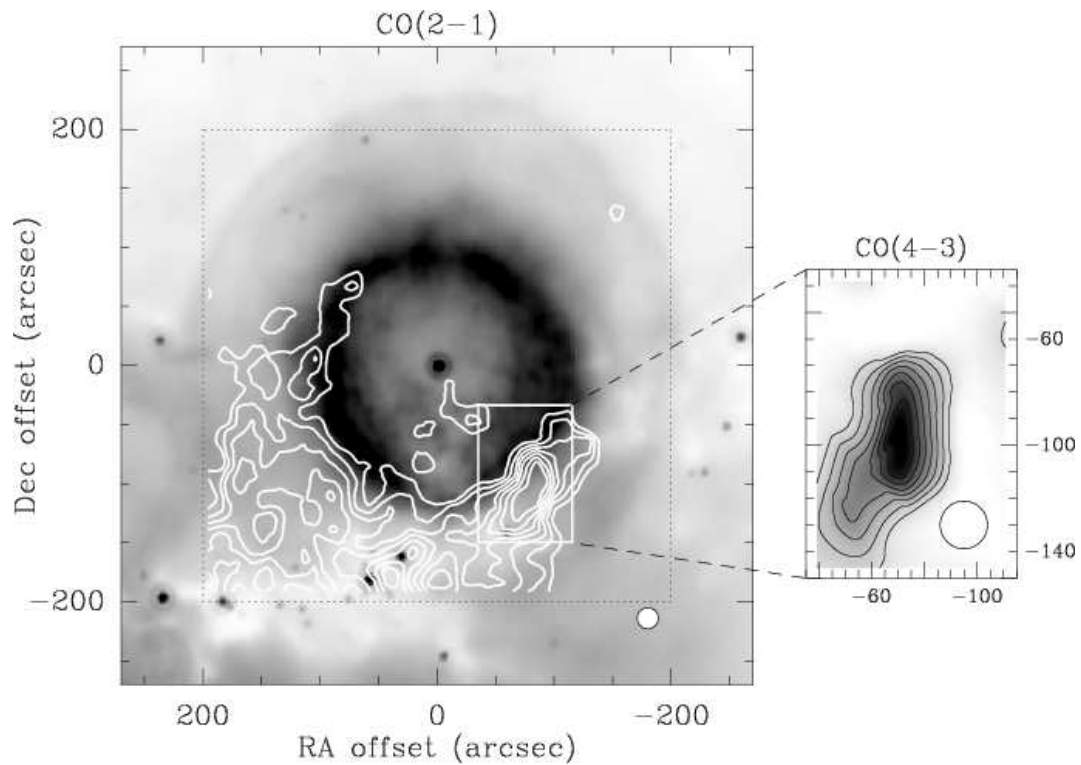
9

Fig. 7.— Same as Figure 6, but in the velocity range from +3.4 to +4.0 km s^{-1}. *Left:* contours are 30 % – 90 % of the peak value (10.8 K in T_A^* scale), in steps of 10 %. *Right:* contours are 25 % – 95 % of the peak value (3.4 K in T_A^* scale), in steps of 10 %. This velocity range corresponds to a shocked clump reported in Paper I. After increasing the angular resolution, a second, outer shell is clearly visible in both lines.

The SED of the central object (upper panel) shows that the flux decreases from 5 to about $19 \, \mu$m and increases again to longer wavelengths. This behavior may be roughly explained by two emitters at two different temperatures, i.e., hotter (shorter wavelengths) and colder material (longer wavelengths). The middle and lower panels of Figure 3 correspond to the spectra of the shell and the IRDC, respectively. These two last SEDs are dominated by the colder component.

The three SEDs present an astonishing similarity for $\lambda > 25 \, \mu$m. This suggests that this emission is due to interstellar material which is present in all regions and extends beyond the observed area.

Figure 2 shows the position of the IRS spectra slits for the three regions observed. It is clear that the SL and LL spectra of the central object are affected by the shell emission. The effect is maximum at longer wavelengths, since the emission of the shell at shorter wavelengths is negligible when compared with the emission of the central object (see Figure 3). Thus, in order to remove the contribution of the shell emission to the central object SED, we have scaled the LL spectrum of the shell to fit that of the central object at the longest wavelengths ($> 32 \, \mu$m) and later subtracted from the last one. The result is shown in Figure 3 (upper panel) with a solid line. The subtracted central object SED shows the decreasing tail of the central object emission. In addition, several spectral lines ([Ne III] at $15.5 \, \mu$m, [S III] at 18.71 and $33.4 \, \mu$m, H_2 at $28.2 \, \mu$m, and [S III] at $34.8 \, \mu$m) have disappeared of the central object spectrum.

4.3.1. Solid-state Features

The SEDs of the central object and the IRDC reveal an absorption feature at around $9.7 \, \mu$m, more prominent in the case of the central object, particularly clear after subtracting the shell contribution (Figures 3 and 4). It corresponds to the well-known $9.7 \, \mu$m amorphous silicates feature due to the Si–O stretching in the dust grains. The presence of amorphous silicates was also reported in the dusty nebula surrounding the LBV stars HR Car (Lamers et al. 1996a; Umana et al. 2009) and Wra 751 (Voors et al. 2000a). Note, however, that these stars present the feature in emission instead of absorption as in the case of G79.29+0.46, which is puzzling and has to be explained. In addition, the SED of the shell seems to present a shallow depression at around $9.7 \, \mu$m that could be interpreted as a weak absorption due to amorphous silicate dust.

The broad, strong emission features at 6.2, 7.7, 8.6, 11.3, and 12.7μm present in the SL spectrum of the shell (See Figure 4, upper panel) are due to vibrational modes of free-flying PAHs (Leger & Puget 1984; Allamandola et al. 1985). The same features seem to appear in the spectrum of the IRDC, but the flux is too low for reliable detections. These PAHs features suggest the presence of very small C rich dust grains or molecules in the shell of G79.29+0.46. PAHs have also been detected in the shell of the galactic LBV stars AG Car (Voors et al. 2000a) and HR 168625 (Skinner 1997), and in the LBV star R71 of the Large Magellanic Cloud (Voors et al. 1999).

Another interesting solid-state feature, present only in the spectrum of the IRDC, is the CO_2 bending mode at about $15 \, \mu$m (see Figure 3, lower panel). Since the formation and evolution of interstellar ices is strongly dependent on local conditions, the presence of CO_2 ice in the spectrum of the IRDC indicates that the physical conditions are rather different from those in the central object and in the shell. CO_2 ice has never been detected in the surroundings of a massive evolved star, but is usual in other astronomical objects, such as high- and intermediate-mass protostars (Ehrenfreund et al. 1998; Peeters et al. 2002; Lefloch et al. 2008). The CO_2 absorption feature found could be coming either from the quiescent regions of the IRDC (south of the LBV nebula) or from the compact source lying within the southern slit (see Figure 2). Note that this compact source was reported as a young stellar object by Redman et al. (2003).

4.3.2. Emission lines

The IRS high-resolution spectra of the central object are full of fine structure lines that may provide important constraints to the physical conditions in the region. The most prominent ones are also detected in the low-resolution spectra and are labeled in the figures. For each line, a first-order baseline has been defined and the line has been fitted to a Gaussian. To do this, we have used an iterative software developed by Bayo (2009). The identification and the measured fluxes are summarized in Table 2, including possible multiple iden-

tifications. Flux errors are between brackets. All line fluxes for the central object have been measured in the high-resolution IRS spectra but H I at $7.46\,\mu$m. In the case of the shell and the IRDC, line fluxes have been measured in the respective low-resolution IRS spectra. There is a mismatch between the SH and LH spectra of the central object which is usually attributed to a difference in the two module apertures, and which has been taken into account when comparing fluxes of SH with those of LH spectra.

The collection of spectral lines found is similar to that shown by the LBV star HR Car (Umana et al. 2009) and the LBV candidate HDE 316285 (Morris, P., et al. 2008). The nebular spectra of HDE 316285 show, for the first time in this kind of objects, pure rotational lines of H_2 arising from optically thin quadrupole transitions, from S(0) to S(6). We have also clearly detected the two lower rotational lines, S(0) and S(1), in the spectra of the central object and the shell, and S(0) in the spectrum of the IRDC. Although these lines may arise from a foreground component, or even DR 15, the presence of H_2 in the shell or in the circumstellar material is a possibility which has to be explored in follow-up observations.

5. Discussion

5.1. Multiple shells in G79.29+0.46

The data shown in this paper clearly show multiple dust and gas shells connected to the central star of G79.29+0.46. The MIPS $24\,\mu$m image shows two well-defined dust shells. Figure 6 shows how the CO shell coexists next to the inner dusty shell, while Figure 7 shows another slab located between the two dust shells.

To explore the possibility of the existence of a more inner shell closer to the LBV star, we have roughly fitted the SED of the central object after subtracting the contribution of the shell with a combination of two blackbodies. Two ranges of temperatures were tried, from 10,000 to 30,000 K for the stellar contribution and from 200 to 1500 K for a possible inner envelope. Fitting does not vary significantly in the considered ranges of temperature corresponding to the hotter blackbody. However, the best fit regardless the stellar temperature was always obtained with a second blackbody of ~ 900 K. This result is compatible with the exis-

tence of an inner shell unresolved by the Spitzer images. Figure 3 shows the best fit for a stellar temperature of 20,000 K. This conclusion is supported by the detection of H_2 lines in the spectra of the central object. It is necessary a thick dust envelope to be able to explain the existence of H_2 so close to the LBV star. This thick dust envelope would shield the molecule gas from the strong UV field of the star.

From the morphology, it seems that the two dusty shells resolved by the Spitzer images are interacting with the surrounding medium (see Figure 1), presumably with material belonging to the DR 15 cloud. Figure 7 also shows clear evidence of the erosion of the ISM by the stellar wind, specially at the southwestern region. At this region, we already reported in Paper I the presence of a shock front.

In Paper I, we estimated an age of the nebula between 10^3 and 10^4 yr. This is in well agreement with the high sphericity shown by the two dust shells. Thus, the mass-loss events which have produced the multiple shells have occurred relatively recently, i.e., in the current evolutionary stage.

In order to obtain a dust temperature, we have also fitted the continuum emission of the shell and the IRDC, with a combination of two blackbodies at different temperatures. In the case of the shell, a blackbody of 65 K and another of 132 K were necessary. For the IRDC, one of 66 K and another of 187 K were used. The resulting fits are shown in Figure 3. In both cases, two dust components at different temperatures were found, one common component at ~ 65 K and another hotter. Probably, the cold component is due to foreground interstellar material belonging to the H II region DR 15, as typical dust temperatures of H II regions are around $60-70$ K (Peeters et al. 2002). This is the main dust component and would explain why both spectra have the same overall shape at longer wavelengths. Regarding the hot component of the shell, its temperature is similar (same order) to the temperatures estimated for the dust in other LBV nebulae (300 K; Voors et al. 1999) and in supernova remnants (SNRs) associated with shocks (~ 110 K; Tappe et al. 2006; Ghavamian et al. 2009). Note that the temperature of the hot component of the shell is slightly lower than the temperature of the hot component of the IRDC. Although these temperatures should

TABLE 2

LINE IDENTIFICATION AND MEASURED FLUXES

Line	λ^a	Flux ($10^{-14}\,\mathrm{erg\,cm^{-2}\,s^{-1}}$)		
	(μm)	The Central Object	The Shell	The IRDC
[Ar II]; [Ne II]	6.97		7.7 (0.6)	
H I 6-5 8-6	7.46	960 (90)		
[Ar III]	8.99		6 (2)	
He II 10-9	9.67			2.6 (0.8)
He II 24-16; H I 12-8; [S IV]	10.50	19 (3)		
[Ni II]	10.68	7.7 (0.6)		
[Ne III]	10.88	16 (2)		
He II 23-16 18-14; [Ni I]; H I 9-7	11.30	28 (2)	58 (8)^b	
H I 15-9	11.53	8 (2)		
He II 14-12; H I 7-6	12.37	77 (7)		1.9 (0.2)
[Ne II]	12.81	18 (2)	98 (8)^b	4.6 (0.2)^b
H I 17-10; H I 11-24	13.93	6.7 (1.0)		
H I 13-9	14.17	5.1 (0.6)		
H I 23-11	14.29	3.0 (1.0)		
H I 16-10	14.94	6.7 (1.3)		
[Ne III]	15.55	13 (2)	29 (3)	
He II 20-16; H I 10-8	16.20	10 (2)		
He II 24-18; H I 12-9	16.87	3.6 (0.3)		
H$_2$ 0-0 S(1)	17.03	4.0 (0.5)	19 (6)	
H I 18-11	17.60	6.7 (2)		
[Fe II]	17.90	8.4 (0.4)		
S III	18.71	24.0 (1.0)	184 (15)	18 (4)
He II 23-18 16-14; H I 8-7	19.05	24 (5)		
H I 20-12	20.52	4.5 (0.6)		
[Ar III]	21.82	5.2 (0.6)		
He II 17-15; H I 13-10 11-9	22.32	27 (2)		
H I 15-11	23.86	27.0 (1.4)		
[F I]	24.75	9.0 (0.5)		
H I 21-13	24.98	4.1 (0.8)		
[Fe II]	25.97	23 (3)		
H I 24-14	27.08	7.3 (0.5)		
He II 18-16; H I 9-8	27.79	29 (2)		
H$_2$ 0-0 S(0)	28.21	13 (4)	25 (6)	11 (2)
H I 14-11	28.85	7.7 (0.8)		
H I 19-13	28.97	14 (3)		
He II 24-20; H I 12-10	29.83	10.3 (0.7)		
[S III]	33.45	78 (11)	740 (40)	229 (15)
[Si II]	34.80	41.5 (1.1)	150 (40)	66 (6)

[a] Peak wavelength measured on the stellar spectrum.

[b] Flux measured affected by PAHs emission.

13

be seen with caution due to the presence of the CO_2 ice absorption feature, the slightly higher temperature in the IRDC could be due to the presence of a young stellar object in the slit (see Figure 2).

The most external dust shell is only visible in the $24\,\mu$m image. It is expected that the dust in this shell would have a lower temperature than the dust in the inner shells. Thus, the dust temperature of the most external shell should not be well above $120\,$K. Assuming that the mid-infrared images are tracing the thermal continuum emission of the dust, this would explain why it is not detected at shorter wavelengths. The fact that this shell is neither detected at $70\,\mu$m could be due to a combination of strong foreground/background emission at this wavelength, lower sensitivity of MIPS in this band, and a non-appropriate data reduction of the image.

The $9.7\,\mu$m amorphous silicates feature in absorption is clearly present in the SL spectra of the central object and the IRDC, and is tentatively detected in the shell. Amorphous silicates in LBV stars are supposed to be formed at temperatures well below the silicates melting point in the outer layers of the star which cool very rapidly while the material is being swept up by a fast wind. The silicates would indicate that the stellar ejecta was oxygen rich ($C/O < 1$), as expected for LBV stars which are supposed to have ejecta enriched by the CNO cycle (Nota et al. 1997). However, G79.29+0.46 shows the $9.7\,\mu$m amorphous silicates feature in absorption instead of in emission as the others LBV stars do. A plausible explanation is that the absorption of amorphous silicates is due to the foreground ISM, as was recently found in the case of the SNR N157B by Micelotta et al. (2009). This would explain the presence of this feature in absorption in the IRDC as well. However, another possible explanation for the absorption shown in the central object spectrum is the presence of amorphous silicate dust in an inner nebula unresolved by the Spitzer images.

The presence of crystalline silicates in LBV nebulae seems to be a general trend (Waters et al. 1997). This is suggestive of the grains being formed in high-density and low-temperature environments (Voors et al. 1999). Therefore, and because these features resemble those observed in red supergiant stars, the presence of crystalline silicates is explained if the dust is formed in high-density, slow-expanding environments close to the star, rather than in the swept-up shell. This kind of environment is typical of the red supergiant phase (Waters et al. 1998), for which wind velocities are between 20 and $30\,\mathrm{km\,s^{-1}}$. In the case of G79.29+0.46, and similarly to the LBV candidate HDE 316235 (Morris, P., et al. 2008) and the LBV stars η Carina and HR Car (Umana et al. 2009), its spectrum does not show any signature of crystalline silicates. The lack of crystalline silicates could be explained if the nebular material was rapidly ejected and could not crystallize under conditions of rapid cooling and low monomer densities, as suggested by Morris, P., et al. (2008) for HDE 316235. Another possible explanation would be amorphization of initially crystalline dust, which may occur under heavy proton bombardment due to the stellar wind. This last mechanism also explains the lack of crystalline silicates in the ISM (Carrez et al. 2002; Brucato et al. 2004).

5.2. Features of ionized nebulae

Ratios of fine structure lines can be compared with typical values found toward H II regions, photo-dissociation regions (PDRs), SNR, and the ISM. First, we have considered the ratio between [Si II] $34.8\,\mu$m and [S III] $33.5\,\mu$m. Theseq two lines are found in the ISM, and their ratio is indicative of the degree of excitation of the gas. According to Simpson et al. (2007), this line ratio is ~ 2.5 for the diffuse interstellar gas, and just in the range $0.1 - 0.6$ toward H II regions. Since the values estimated for the G79.29+0.46 region are similar to those of H II regions (0.3 for the IRDC, 0.2 for the shell, and 0.5 for the central object), this suggests that the three components studied in this work have important amount of ionized gas. While this was expected for the shell and the central object, where free–free thermal emission was already detected (Higgs et al. 1994), we note that the IRDC component is most likely picking some emission from the H II region DR 15, which is located only $4'$ to the (south) east of the LBV star and is covered by the IRS slit.

Similarly, a correlation was found for the ratio between [Ne III] $15.5\,\mu$m and [Ne II] $12.8\,\mu$m, and the ratio between [S IV] $10.5\,\mu$m and [S III] $18.7\,\mu$m (Martín-Hernández et al. 2002). Such a correlation can be used to measure the de-

gree of ionization of a region. For the case of the central object, the first ratio is around 0.7, and the second is around 0.8 (assuming no contamination from He II and H I at the [S IV] line). By placing this value in the diagram ([Ne III]/[Ne II] versus [S IV]/[S III]) of Figure 1 of Martín-Hernández et al. (2002), we have found that the central object lies in an intermediate case between the H II regions with low and high ionization, and in particular it is close to the value of the Orion Nebula. In addition, we have measured the ratio between [Ne III] $15.5\,\mu$m and [Ne II] $12.8\,\mu$m for the shell and have found a value around 0.3. It is interesting to note the finding of Ghavamian et al. (2009) that slow and dense shocks produce a ratio around 0.4, which is very similar to the value found in the shell of G79.29+0.46. This suggests the presence of slow shocks in the shell, which is completely consistent with the recent discovery of a slow CO shock in the southwestern side of the shell of G79.29+0.46 (Paper I).

Finally, from the ratio between [S III] $33.4\,\mu$m and [S III] $18.7\,\mu$m, one can make a rough estimate of the electron density. The ratio[3] is 1.1, 4.0, and 13.0 for the central object, the shell, and the IRDC, respectively. The ratio of ~ 1 corresponds to an electron density of ~ 500 cm^{-3} (Rubin 1989; Rubin et al. 1994). These values are consistent with the electron density of ~ 1000 cm^{-3} derived by Umana et al. (2009) for the central object of HR Car. For the shell and the IRDC, this ratio is too high to be able to derive a reliable electron density. This could be indicative of strong extinction for the shell and the IRDC cases, as found for some positions in the galactic center by Simpson et al. (2007).

5.3. PDR signatures

PAH emission features are present in the SL spectrum of the shell. This dust material was also detected in the LBV stars AG Car,

---

[3]To compute this ratio, we have corrected the line intensity at $18.7\,\mu$m by a factor of 3. This factor for aperture losses applies only to the central object, for which the flux densities have been calculated in the high-resolution spectra, and the line at $18.7\,\mu$m falls in a different module than the line at $33.4\,\mu$m. For the shell and the IRDC, there is no need of correction because both lines fall in the same module.

HR 168625, R71 (Voors et al. 2000b; Skinner 1997; Voors et al. 1999). PAH emission is supposed to be formed where shocks act upon cold molecular gas. This is presumably the situation of G79.29+0.46, where the ionized gas is interacting with the molecular material traced by CO. Note that the presence of shocks is supported by the morphology (see Figures 1, 6, and 7) and by the detection of the CO $J = 4 \rightarrow 3$ line, which has a critical density of at least several 10^4 cm^{-3}.

On the other hand, the spectra of the central object show [Fe II] lines, whereas the same lines are not detected in the IRDC spectra. These two observational findings would indicate that the Fe abundance close to the star is higher than in the surrounding ISM. In the ISM, Fe is highly depleted from the gas phase because of condensation onto dust grains, but shocks would reprocess these dust grains and release Fe atoms into the gas phase. Therefore, a high abundance of Fe in comparison with the ISM would be another evidence of the presence of shocks close to the LBV star.

The presence of PAHs in the spectrum of the shell, the detection of low-excitation fine structure lines such as $26.0\,\mu$m [Fe II] in the central object spectrum, and the CO gas emission, point out to the existence of a PDR surrounding the ionized part of the nebula. Laurent et al. (2000) showed a typical spectrum of a star-forming region, an H II region, and a PDR (see their Figures 1 and 2). In our case, the spectrum of the shell shown in Figure 4 is an intermediate case between a PDR and an H II region. In addition, the non-detection of [S I] at $25\,\mu$m and the detection of [S III] are characteristic of photon-ionized gas (Micelotta et al. 2009). In fact, [S III] and [Si II] are typical PDR tracers (Tappe et al. 2006; Umana et al. 2009), along with [Ar III], [Ne II], [Ne III], and [S IV] (e.g., Martín-Hernández et al. 2002; Compiègne et al. 2008; Ghavamian et al. 2009), all present in the central object spectra.

In PDRs, PAHs are non-thermally excited by single ultraviolet (UV) photons (Sellgren 1984), and far-UV photons control both the thermal and chemical structure of the neutral gas (Tielens & Hollenbach 1985). The high values of both the stellar effective temperature ($T_{\rm eff}$) and luminosity (L_*) favor the presence of a PDR where the significant UV field encounters cold molecular gas. However, as the CO shells are at large stellar

distances, the presumably high UV field may be diluted.

Thus, we have made an attempt to estimate the incident UV field (G_0) in the $24\,\mu$m inner shell. G_0 is defined as the fraction of an incident UV field in the ionizing UV range (i.e., between 6 and 13.6 eV). This is usually expressed in units of the Habing field ($1.2 \times 10^{-4}\,\mathrm{erg\,cm^{-2}\,s^{-1}\,sr^{-1}}$), which is a representative value of the mean interstellar UV field. G_0 depends on the stellar parameters as

$$G_0 \propto f_{\mathrm{UV}}(T_{\mathrm{eff}}) \cdot L_* \cdot d^{-2}, \qquad (1)$$

where d is the distance of the affected volume to the star and f_{UV} is the fraction of the Planck function emitted between 6 and 13.6 eV with respect to the total:

$$f_{\mathrm{UV}}(T_{\mathrm{eff}}) = \frac{\int_{6\,eV}^{13.6\,eV} B_\nu(T_{\mathrm{eff}})}{\int_0^\infty B_\nu(T_{\mathrm{eff}})}. \qquad (2)$$

By varying T_{eff} between 15,000 and 30,000 K, and L_* between 1 and $2 \times 10^5\,\mathrm{L_\odot}$, G_0 ranges from 0.8 to 3.0×10^4, in units of Habing field. In the assumed range of T_{eff}, f_{UV} varies from 31% to 56% of the total energy emitted by the star. A value for d of 1 pc was assumed, which corresponds to the distance of the $24\,\mu$m shell to the star, at a distance of 1.7 kpc.

These high values of G_0 (of the order of 10^4), together with moderately high H_2 densities (at least several $10^4\,\mathrm{cm^{-3}}$ due to the presence of CO $J = 4 \to 3$), are similar to the conditions found in extreme PDRs, such as the well-known Mon R2 (Rizzo et al. 2003a; Berné et al. 2009). It is also compatible with the values found by Umana et al. (2009) in HR Car. However, PAHs are expected to be not widespread but located in small regions where the restrictive conditions of PDRs apply. A zone close to the inner $24\,\mu$m shell and the CO $J = 4 \to 3$ shells is a good candidate to search for these fragile large molecules.

5.4. Molecular hydrogen

The 0–0 S(0) line of H_2 has been detected in the three targets, while the S(1) line has only been identified in the central object and the shell. Unfortunately, we have not detected more excited pure rotational lines (S(2) and above), which prevent us a thorough excitation study. Despite that,

the mere presence of molecular hydrogen in the close environs of a LBV star is interesting and deserves further analysis. To the best of our knowledge, the only reported detection of H_2 close to a LBV was done by Morris, P., et al. (2008). It is important to note that Umana et al. (2009), using similar data sets than ours, did not found any H_2 lines in the dusty nebula HR Car.

Vibrationally excited H_2 was also discovered surrounding part of the Wolf-Rayet nebula NGC 2359 (St-Louis et al. 1998), in correlation with significant amounts of (probably) shocked CO (Rizzo et al. 2001, 2003b).

Our values of the S(1)/S(0) line ratio are not too different to those found by Tappe et al. (2006) in a molecular cloud to an SNR, affected by both UV radiation and shocks. Unfortunately, a deeper analysis from this line ratio is not appropriate due to the fact that both lines correspond to different species, and we cannot constrain the ortho-to-para ratio. A better study including more lines and a precise spatial distribution may help to understand the nature of the emitting H_2 lines, as well as a comparison to several PDR models (see, e.g. Draine & Bertoldi 1996; Compiègne et al. 2008)

6. Conclusions

In order to shed light on the distribution of warm dust, PAHs and CO gas in G79.29+0.46, we have analyzed infrared Spitzer data and observed the CO $J = 2 \to 1$ and $4 \to 3$ lines using the IRAM 30m radio telescope and the SMT.

An analysis of the high-sensitivity MIPS $24\,\mu$m image has led us to the discovery of a second outer dusty shell with a spherical shape, previously overlooked. In addition, the analysis of the SED of the central object has revealed the possible existence of a third extremely young dust shell closer to the LBV star, unresolved in the Spitzer images. Furthermore, the new CO data shown in this paper have revealed two separated gaseous shells located between the two dusty shells. The dynamic time of these gaseous components would indicate that the various shells have been formed during the current evolutionary stage. The presence of multiple shells around a LBV star is of great interest because its implications for stellar evolution theories. This would indicate that the mass-loss history has been more complex than previously assumed, with

periods of enhanced and dimmed stellar winds instead of a continuous steady one.

Using the IRS low-resolution spectra, we have compared three regions in the field of G79.29+0.46: the central object, the shell, and the IRDC. The three studied regions present a clear similarity at the longest wavelengths ($> 25\,\mu$m), due to the presence of a large amount of foreground/background dust at ~ 65 K. A rich variety of solid-state features has been detected. Amorphous silicate features in absorption are present in the spectra of the central object and the IRDC, probably due to the foreground ISM and/or to the presence of amorphous silicate dust in a likely inner nebula very close to the central LBV star. PAHs features in emission are present in the spectrum of the shell, and a tentative detection of amorphous silicate in absorption is reported as well. Furthermore, a CO_2 ice feature in absorption is present in the spectrum of the IRDC.

The IRS high-resolution spectra of the central object are full of fine structure lines, similar to those detected in other LBV stars. We have also detected pure rotational lines of H_2 arising from optically thin quadrupole transitions in two regions of G79.29+0.46, the central object and the shell, which is the first detection of H_2 in the spectrum of a LBV star.

Using different flux line ratios, we have analyzed the physical conditions of G79.29+0.46 and its surroundings. In the case of the shell, indications of slow shocks have been found.

We have estimated an incident UV field in the inner dusty shell of the order of 10^4 in units of Habing field. This high value of G_0, together with other evidence such as moderately high H_2 densities, the presence of PAHs in the shell, the detection of low-excitation fine structure lines, and the CO mid-J emission, suggests the existence of a PDR.

This study of the multiple phase material directly associated with G79.29+0.46 may help to understand its recent past and consequently the evolutionary mechanisms of this kind of object. In this sense, G79.29+0.46 becomes a paradigm of LBV nebula and deserves further studies. In particular, a follow-up study of complex molecules should also be carried out, because they can provide information about the physical parameters in detail. In addition, similar studies to the one shown in this paper for other LBVs and evolved massive stars will also help to understand this short, but crucial, evolutionary phase of high-mass stars.

REFERENCES

Allamandola, L. J., Tielens, A. G. G. M., & Barker, J. R. 1985, ApJ, 290, L25

Baars, J. W. M., Martin, R. N., Mangum, J. G., McMullin, J. P., & Peters, W. L. 1999, PASP, 111, 627

Bayo, A. 2009, PhD thesis, Universidad Autónoma de Madrid, Spain

Berné, O., Fuente, A., Goicoechea, J. R., Pilleri, P., González-García, M., & Joblin, C. 2009, ApJ, 706, L160

Brucato, J. R., Strazzulla, G., Baratta, G., & Colangeli, L. 2004, A&A, 413, 395

Carrez, P., Demyk, K., Cordier, P., Gengembre, L., Grimblot, J., D'Hendecourt, L., Jones, A. P., & Leroux, H. 2002, Meteorit. Planet. Sci., 37, 1599

Clark, J. S., Larionov, V. M., & Arkharov, A. 2005, A&A, 435, 239

Compiègne, M., Abergel, A., Verstraete, L., & Habart, E. 2008, A&A, 491, 797

Draine, B. T., & Bertoldi, F. 1996, ApJ, 468, 269

Egan, M. P., Clark, J. S., Mizuno, D. R., Carey, S. J., Steele, I. A., & Price, S. D. 2002, ApJ, 572, 288

Egan, M. P., Shipman, R. F., Price, S. D., Carey, S. J., Clark, F. O., & Cohen, M. 1998, ApJ, 494, L199

Ehrenfreund, P., Dartois, E., Demyk, K., & D'Hendecourt, L. 1998, A&A, 339, L17

Fazio, G. G., et al. 2004, ApJS, 154, 10

Ghavamian, P., Raymond, J. C., Blair, W. P., Long, K. S., Tappe, A., Park, S., & Winkler, P. F. 2009, ApJ, 696, 1307

Gvaramadze, V. V., Kniazev, A. Y., & Fabrika, S. 2009, arXiv e-prints

Higgs, L. A., Wendker, H. J., & Landecker, T. L. 1994, A&A, 291, 295

Houck, J. R., et al. 2004, ApJS, 154, 18

Humphreys, R. M., & Davidson, K. 1994, PASP, 106, 1025

Kutner, M. L., & Ulich, B. L. 1981, ApJ, 250, 341

Lamers, H. J. G. L. M., et al. 1996a, A&A, 315, L225

—. 1996b, A&A, 315, L229

Laurent, O., Mirabel, I. F., Charmandaris, V., Gallais, P., Madden, S. C., Sauvage, M., Vigroux, L., & Cesarsky, C. 2000, A&A, 359, 887

Lefloch, B., Cernicharo, J., & Pardo, J. R. 2008, A&A, 489, 157

Leger, A., & Puget, J. L. 1984, A&A, 137, L5

Martín-Hernández, N. L., Vermeij, R., Tielens, A. G. G. M., van der Hulst, J. M., & Peeters, E. 2002, A&A, 389, 286

Mauersberger, R., Guelin, M., Martin-Pintado, J., Thum, C., Cernicharo, J., Hein, H., & Navarro, S. 1989, A&AS, 79, 217

Micelotta, E. R., Brandl, B. R., & Israel, F. P. 2009, A&A, 500, 807

Morris, P., et al. 2008, in IAU Symp. 250, Massive Stars as Cosmic Engines, ed. F. Bresolin, P. A. Crowther, & J. Puls, (Cambridge: Cambridge Univ. Press), 361

Nota, A., Pasquali, A., Marston, A. P., Lamers, H. J. G. L. M., Clampin, M., & Schulte-Ladbeck, R. E. 2002, AJ, 124, 2920

Nota, A., Smith, L., Pasquali, A., Clampin, M., & Stroud, M. 1997, ApJ, 486, 338

Oka, T., et al. 2001, ApJ, 558, 176

Peeters, E., et al. 2002, A&A, 381, 571

Redman, R. O., Feldman, P. A., Wyrowski, F., Côté, S., Carey, S. J., & Egan, M. P. 2003, ApJ, 586, 1127

Rieke, G. H., et al. 2004, ApJS, 154, 25

Rizzo, J. R., Alfonso, J., & Ortiz, E. 2008a, in ASP Conf. Ser., Vol. 388, Mass Loss from Stars and the Evolution of Stellar Clusters, ed. A. de Koter, L. J. Smith, & L. B. F. M. Waters (San Francisco, CA: ASP), 219

Rizzo, J. R., Fuente, A., Rodríguez-Franco, A., & García-Burillo, S. 2003a, ApJ, 597, L153

Rizzo, J. R., Jiménez-Esteban, F. M., & Ortiz, E. 2008b, ApJ, 681, 355

Rizzo, J. R., Martín-Pintado, J., & Desmurs, J. 2003b, A&A, 411, 465

Rizzo, J. R., Martín-Pintado, J., & Mangum, J. G. 2001, A&A, 366, 146

Rubin, R. H. 1989, ApJS, 69, 897

Rubin, R. H., Simpson, J. P., Lord, S. D., Colgan, S. W. J., Erickson, E. F., & Haas, M. R. 1994, ApJ, 420, 772

Schuster, K.-F., et al. 2004, A&A, 423, 1171

Sellgren, K. 1984, ApJ, 277, 623

18

Simpson, J. P., Colgan, S. W. J., Cotera, A. S., Erickson, E. F., Hollenbach, D. J., Kaufman, M. J., & Rubin, R. H. 2007, ApJ, 670, 1115

Skinner, C. J. 1997, in ASP Conf. Ser., Vol. 120, Luminous Blue Variables: Massive Stars in Transition, ed. A. Nota & H. Lamers (San Francisco, CA: ASP), 322

Smith, N. 2007, AJ, 133, 1034

Smith, N., Brooks, K. J., Koribalski, B. S., & Bally, J. 2006, ApJ, 645, L41

Smith, N., & Owocki, S. P. 2006, ApJ, 645, L45

St-Louis, N., Doyon, R., Chagnon, F., & Nadeau, D. 1998, AJ, 115, 2475

Tappe, A., Rho, J., & Reach, W. T. 2006, ApJ, 653, 267

Tielens, A. G. G. M., & Hollenbach, D. 1985, ApJ, 291, 722

Umana, G., Buemi, C. S., Trigilio, C., Hora, J. L., Fazio, G. G., & Leto, P. 2009, ApJ, 694, 697

Voors, R. H. M., Geballe, T. R., Waters, L. B. F. M., Najarro, F., & Lamers, H. J. G. L. M. 2000a, A&A, 362, 236

Voors, R. H. M., Waters, L. B. F. M., Morris, P. W., Trams, N. R., de Koter, A., & Bouwman, J. 1999, A&A, 341, L67

Voors, R. H. M., et al. 2000b, A&A, 356, 501

Waters, L. B. F. M., Izumiura, H., Zaal, P. A., Geballe, T. R., Kester, D. J. M., & Bontekoe, T. R. 1996, A&A, 313, 866

Waters, L. B. F. M., Morris, P. W., Voors, R. H. M., & Lamers, H. J. G. L. M. 1997, in ASP Conf. Ser., Vol. 120, Luminous Blue Variables: Massive Stars in Transition, ed. A. Nota & H. Lamers (San Francisco, CA: ASP), 326

Waters, L. B. F. M., Morris, P. W., Voors, R. H. M., Lamers, H. J. G. L. M., & Trams, N. R. 1998, Ap&SS, 255, 179

Werner, M. W., et al. 2004, ApJS, 154, 1